Estimating the masses of Narrow line Seyfert 1 galaxies using damped random walk method

Rachana, 1,2 M. Vivek 20t, Yue Shen^{3,4} to

¹ Joint Astronomy Programme, Department of Physics, Indian Institute of Science, Bangalore 560012, India;

Accepted XXX. Received YYY; in original form ZZZ

ABSTRACT

Narrow-line Seyfert 1 galaxies (NLSy1s) are a subclass of active galactic nuclei (AGNs), commonly associated with rapidly accreting, relatively low-mass black holes ($10^6-10^8M_{\odot}$) hosted in spiral galaxies. Although typically considered to have high Eddington ratios, recent observations, particularly of γ -ray-emitting NLSy1s, have raised questions about their true black hole masses, with some estimates approaching those of Broad-line Seyfert 1 (BLSy1) systems. In this work, we present the recalibrated mass estimations for a large sample of NLSy1s galaxies with z < 0.8. We apply the damped random walk (DRW) formalism to a comparison set of 1,141 NLSy1 and 1,143 BLSy1 galaxies, matched in redshift and bolometric luminosity using SDSS DR17 spectroscopy. Our analysis employs a multivariate calibration that incorporates both the Eddington ratio and the rest-frame wavelength to refine the mass estimates. We obtain median DRW-based black hole masses of $\log(M_{\rm BH}^{\rm DRW}/M_{\odot}) = 6.25 \pm 0.65$ for NLSy1s and 7.07 ± 0.67 for BLSy1s, in agreement with their respective virial mass distributions. Furthermore, we identify strong inverse trends between the variability amplitude and both optical luminosity and Fe II emission strength, consistent with a scenario where higher accretion rates suppress long-term optical variability. These findings reinforce the view that NLSy1s harbor smaller black holes and highlight the value of variability-based approaches in tracing AGN accretion properties.

Key words: galaxies: active – galaxies: nuclei – galaxies: Seyfert – galaxies: photometry – quasars: supermassive black holes – methods: data analysis

1 INTRODUCTION

Narrow-line Seyfert 1 (NLSy1) galaxies represent a unique subclass of active galactic nuclei (AGN) distinguished by their narrow $H\beta$ emission lines (FWHM $\leq 2000 \text{ km s}^{-1}$) and relatively weak $[O III]\lambda 5007$ emission lines, with a flux ratio of $[O III]\lambda 5007/H\beta \le 3$ (Osterbrock & Pogge 1985; Goodrich 1989). They typically exhibit steeper soft X-ray spectra (E < 2keV), soft X-ray excess, and rapid soft X-ray variability (Boller et al. 1996; Wang et al. 1996; Leighly 1999a,b). These spectral and variability features are found to be significantly correlated. In particular, Boroson & Green (1992), through principal component analysis (PCA), demonstrated that the primary eigenvector (Eigenvector 1) in AGN reflects a strong positive correlation with the strength of Fe II emission, an anti-correlation with the strength of [O III] emission and with the width of broad Balmer lines, highlighting the spectral diversity within AGNs. Later, Shen & Ho (2014) demonstrated the Fe II /H β sequence is indeed correlated with L/L_{Edd} , making the Fe II /H β ratio a reliable albeit empirical indicator for the Eddington ratio. In addition to this, Véron-Cetty et al. (2001) reported that NLSy1 galaxies frequently exhibit an Fe II /H β intensity

* E-mail: rachana2022@iisc.ac.in

ratio exceeding 0.5, reinforcing the role of strong Fe $\scriptstyle\rm II$ emission as a defining characteristic of this subclass.

In addition to their distinctive spectral and X-ray properties, NLSy1s are also distinguished by the physical characteristics of their central engines. Their relatively narrow widths "broad" emission lines imply lower virial velocities, which, when combined with AGN luminosity, suggest comparatively low black hole masses. These scaling relations, commonly referred to as single-epoch (SE) mass estimates, are established using techniques such as reverberation mapping (RM) (Blandford & McKee 1982; Peterson 1993; Cackett et al. 2021), which measures the time delay between variability in the continuum and the response in broad emission lines (Kaspi et al. 2000, 2005; Bentz et al. 2006, 2009, 2013). Applying these methods, numerous studies have found that NLSy1s typically host black holes in the range of 10^6 - 10^8 M_{\odot} , that accrete at high rates, often approaching or exceeding the Eddington limit (Grupe & Mathur 2004; Williams et al. 2018).

Despite their relatively low black hole masses and high accretion rates, a subset of NLSy1 galaxies has been observed to emit γ -rays, indicating the presence of relativistic jets (Abdo et al. 2009; Foschini et al. 2011; D'Ammando et al. 2012; Paliya et al. 2018). This discovery has sparked significant interest, as it challenges the prevailing notion that powerful jets are exclusive to AGNs with massive black holes in elliptical host galaxies. Detailed multi-wavelength analyses,

²Indian Institute of Astrophysics, Block II, Koramangala, Bangalore 560034, India

³Department of Astronomy, University of Illinois at Urbana-Champaign, Urbana, IL 61801, USA

⁴National Center for Supercomputing Applications, University of Illinois at Urbana-Champaign, Urbana, IL 61801, USA

[†] E-mail: vivek.m@iiap.res.in

[‡] shenyue@illinois.edu

particularly in the radio band, along with broadband spectral energy distribution modeling, reveal that these γ -ray emitting NLSy1s share several characteristics with blazars, especially flat-spectrum radio quasars (Paliya et al. 2016, 2018). The key distinction lies in both the host morphology and the inferred black hole mass, as blazars are typically powered by black holes exceeding $10^8~M_{\odot}$ and are hosted by elliptical galaxies, whereas NLSy1s are believed to contain lower-mass black holes within spiral galaxies.

Further evidence challenging virial mass estimates comes from spectro-polarimetric and accretion disk modeling studies. Baldi et al. (2016) estimated a black hole mass of 6×10^8 M_{\odot} for the γ -rayemitting NLSy1 galaxy PKS 2004-447 based on spectro-polarimetric observations, an order of magnitude higher than the 5×10^6 M_{\odot} value obtained from the unpolarised total intensity spectrum. Similarly, Calderone et al. (2013) applied accretion disk model fitting to the spectra of 23 radio-loud NLSy1s (RL-NLSy1s) and found black hole masses comparable to those of blazars. Expanding on this approach, Viswanath et al. (2019) analyzed a sample of ~554 RL-NLSy1 and radio-quiet NLSy1 (RQ-NLSy1) galaxies and compared their mass distributions to a control sample of 471 radio-quiet Broad-line Seyfert 1 (RQ-BLSy1) galaxies. They reported that the mean black hole mass for the NLSy1 sample is systematically higher than values derived from virial estimators. Accretion disk modeling, therefore, provides an alternative method for estimating black hole masses in type-1 AGNs (Capellupo et al. 2015, 2016), while virial estimators remain the standard approach despite their known systematic uncertainties (Mejía-Restrepo et al. 2018). However, the caveat here is that most NLSy1s accrete at high accretion rates ($\dot{m} \ge 0.3$, where $\dot{m} = \frac{\dot{M}}{\dot{M}_{Edd}}$), where the standard thin-disk (Shakura-Sunyaev) model is no longer valid, making accretion disk-based mass estimates less reliable in such cases (Abramowicz et al. 1988; Wang & Netzer 2003).

These discrepancies in virial mass estimates highlight the need for alternative approaches and a critical reassessment of existing methods. One such approach is the damped random walk (DRW) model, a stochastic process that effectively describes the optical variability of quasars and AGNs (Kelly et al. 2009; Kozłowski et al. 2010; MacLeod et al. 2010; Zu et al. 2013). The DRW model appears to be a good description over months to years timescales, but there are likely deviations from the simple DRW behavior on much shorter or much longer timescales (e.g., Stone et al. 2022; Yu et al. 2022). In practice, the DRW model can be implemented as a Gaussian process with an exponential covariance kernel, enabling efficient modeling of light curve variability through a characteristic damping timescale (τ_{DRW}) and amplitude (σ_{DRW}) . In the frequency domain, AGN light curves typically exhibit a power spectral density (PSD) with a slope of -2 at high frequencies and flatten to white noise (slope \rightarrow 0) at low frequencies (Giveon et al. 1999; MacLeod et al. 2010). The transition between these regimes occurs at a characteristic break frequency, defined as $f_{br} = 1/(2\pi\tau_{DRW})$, where τ_{DRW} denotes the variability damping timescale. This timescale has been proposed as a proxy for physical parameters such as black hole mass. Early studies by Collier & Peterson (2001) and Kelly et al. (2009) suggested a connection between this timescale and the physical properties of the central engine, including black hole mass. However, the exact form of this dependence remains uncertain, with several studies reporting inconsistent or weak correlations (e.g., Kozłowski et al. 2010; Simm et al. 2016). More recently, Burke et al. (2021) reported a statistically robust correlation based on a sample of 67 AGNs with high-quality optical light curves, described by:

$$\tau_{\text{DRW}} = 107_{-12}^{+11} \text{ days} \left(\frac{M_{\text{BH}}}{10^8 M_{\odot}}\right)^{0.38_{-0.04}^{+0.05}}$$
 (1)

where $M_{\rm BH}$ is the mass of the supermassive black hole (SMBH) and $\tau_{\rm DRW}$ is the damping timescale characterizing the optical variability. This relation exhibits an intrinsic scatter of $0.33^{+0.11}_{-0.11}$ dex in $M_{\rm BH}$. Notably, this correlation appears to hold across a wide range of accreting systems. It has been extended to the stellar-mass regime through optical variability studies of nova-like accreting white dwarfs (Scaringi et al. 2015). Additionally, Zhang et al. (2024) reported a similar scaling based on a sample of 7 microquasars and 34 blazars observed with the XMM-Newton X-ray Telescope and the Fermi Large Area Telescope, respectively:

$$\tau = 120^{+15}_{-18} \text{ days} \left(\frac{M_{\text{BH}}}{10^8 M_{\odot}} \right)^{0.57 \pm 0.02}$$
 (2)

Beyond black hole mass, several other physical parameters influence the damping timescale $\tau_{\rm DRW}$, including the rest-frame wavelength (λ) and the Eddington ratio ($R_{\rm Edd}$), defined as the ratio of bolometric luminosity to Eddington luminosity (MacLeod et al. 2010; Suberlak et al. 2021; Stone et al. 2022). The dependence of these parameters can be understood in the context of the standard Shakura–Sunyaev accretion disk model (Shakura & Sunyaev 1973). According to this theory, for a given wavelength λ , the characteristic emission region R_{λ} satisfies the condition $k_B T(R_{\lambda}) = hc/\lambda$, where k_B is Boltzmann's constant, h is Planck's constant, c is the speed of light, and $T(R_{\lambda})$ is the disk temperature at radius R_{λ} . This leads to the scaling relation:

$$\frac{R_{\lambda}}{R_{\rm S}} \propto M_{\rm BH}^{-1/3} R_{\rm Edd}^{1/3} \lambda^{4/3},\tag{3}$$

where $R_S = 2GM_{\rm BH}/c^2$ is the Schwarzschild radius and $R_{\rm Edd}$ is the Eddington ratio, defined as

$$R_{\rm Edd} = \frac{L_{\rm bol}}{L_{\rm Edd}} \propto \frac{\dot{M}}{M_{\rm BH}} \tag{4}$$

with $L_{\rm bol}$ being the bolometric luminosity, $L_{\rm Edd}$ the Eddington luminosity, and \dot{M} the mass accretion rate.

In standard accretion disk theory, the thermal timescale (t_{th}) is expected to scale with the black hole mass and the disk radius as follows:

$$t_{\rm th} \approx 1680 \left(\frac{\alpha}{0.01}\right)^{-1} \left(\frac{M_{\rm BH}}{10^8 M_{\odot}}\right) \left(\frac{R}{100 R_{\rm s}}\right)^{3/2} {\rm days},$$
 (5)

where α is the viscosity parameter

In the analysis by Burke et al. (2021), a constant Eddington ratio was assumed across the sample. Under this assumption, the emission radius scales simply with mass as $R_{\lambda} \propto M_{\rm BH}^{2/3}$ and hence, the thermal timescale becomes:

$$t_{\rm th} \propto M_{\rm BH}^{1/2},\tag{6}$$

implying a direct connection between $\tau_{\rm DRW}$ and $M_{\rm BH}$ when Eddington ratio is held fixed. However, for systems with high or variable $R_{\rm Edd}$, this dependence must be explicitly incorporated. For AGNs with high or varying Eddington ratios, it is essential to explicitly account for the influence of $R_{\rm Edd}$ on the thermal timescale. In this regime, the scaling becomes:

$$t_{\rm th} \propto \alpha^{-1} \lambda^2 M_{\rm BH}^{1/2} R_{\rm Edd}^{1/2}.$$
 (7)

Building on this theoretical framework, Zhou et al. (2024) empirically calibrated the dependence of $\tau_{\rm DRW}$ on $M_{\rm BH}$, $R_{\rm Edd}$, and rest-frame

wavelength (λ_{rest}) using a sample of 190 quasars. They derived the following relation based on DRW modeling:

$$\log_{10}(\tau/\text{days}) = a \log_{10}(M_{\text{BH}}/M_{\odot}) + b \log_{10}(R_{\text{Edd}}) + c \log_{10}(\lambda_{\text{rest}}/\text{Å}) + d,$$
(8)

where the best-fitting parameters are $a=0.65\pm0.01$, $b=0.65\pm0.01$, $c=1.19\pm0.01$, and $d=-6.04\pm0.05$ (all at 1σ uncertainty). This multi-parameter calibration demonstrates that $\tau_{\rm DRW}$ is sensitive not only to black hole mass, but also to accretion rate and emission wavelength, especially in high-Eddington ratio systems. In this formulation, the accretion ratio is defined as

$$R_{Edd} = \frac{L_{\rm bol}}{(1+k)L_{\rm Edd}}, \quad k = \frac{1}{3}, \label{eq:Redd}$$

where the factor (1+k) accounts for additional energy dissipation associated with magnetic activity in the corona relative to turbulence within the accretion disk (Sun et al. 2020; Zhou et al. 2024). Motivated by this, we revisit the black hole mass estimates for NLSy1 galaxies, which are known to accrete at high Eddington ratios, often near or above the Eddington limit. Using the DRW framework, we aim to recalibrate $M_{\rm BH}$ for a large sample of NLSy1s by explicitly incorporating the role of accretion rate and comparing the results with their BLSy1 counterparts. Our analysis is based on g-band photometric light curves from the Zwicky Transient Facility (ZTF), including both archival and forced photometry, with sources drawn from the catalog of Paliya et al. (2024). Section 2 details the sample selection and light curve assembly. In Section 3, we describe the DRW modeling approach using the taufit package and the construction of the final analysis sample. Section 4 presents our main results, including updated mass distributions and variability correlations, followed by conclusions in Section 5.

2 SAMPLE SELECTION

We began with an initial sample of 22,656 NLSy1s and 52,273 BLSy1s from the catalog compiled by Paliya et al. (2024), based on spectroscopic data from the Sloan Digital Sky Survey (SDSS) Data Release 17. These sources, classified as either QSOs or GALAXIES by the SDSS pipeline, span redshifts up to z < 0.8. To ensure reliable NLSy1 classification, the catalog required that both the H β and [O III] emission lines be present in the optical spectra, with the FWHM of the broad H β line less than 2000 km/s and a flux ratio [O III] /H $\beta \le 3$ (Osterbrock & Pogge 1985; Goodrich 1989).

For this work, we selected a refined sample of 5,666 NLSy1s and a controlled sample of 5,557 BLSy1s, matched in the Redshift-Luminosity (L–z) plane and limited to sources brighter than 19 magnitudes in the SDSS r band (see Fig. 1). The BLSy1 counterparts were selected such that the matching distance in the L–z plane did not exceed 0.2, resulting in a well-controlled sample with over 98% of NLSy1s successfully matched. The SDSS r-band filter was chosen for the magnitude cut because it has a relatively high throughput, compared to other SDSS filters. To analyze the optical variability of these sources, we utilized light curves from both the archival ZTF survey and the ZTF forced photometry dataset (Masci et al. 2023). The forced photometry data provide a significantly greater number of epochs and a longer observational baseline than the archival data, thereby improving the robustness and reliability of the DRW model fitting.

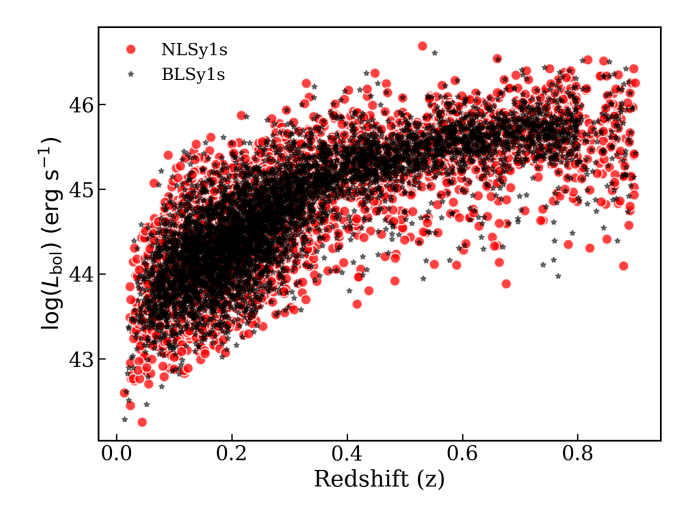
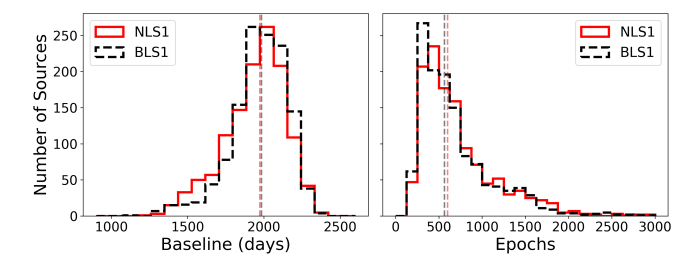


Figure 1. Distribution of the refined sample of NLSy1s (Red) and their matched BLSy1 counterparts (Black) in the luminosity–redshift (L–z) plane. All sources have SDSS r-band magnitudes ≤ 19 and were selected from the catalog of Paliya et al. (2024). The BLSy1 sample was matched using a maximum distance of 0.2 in the L–z plane.

2.1 Photometric Data

We retrieved the light curves for our final sample from the Infrared Science Archive (IRSA) at IPAC, using the most recent public data release (DR23) of the ZTF survey (Graham et al. 2019; Bellm et al. 2019; Masci et al. 2019). The data were obtained using a positional search radius of 1 arcsec, which also includes intranight observations from overlapping field IDs. ZTF is a new optical time-domain survey conducted primarily with the 48-inch Samuel Oschin Schmidt telescope at the Palomar Observatory. It employs a custom-built widefield camera with a field of view of 47 deg² and observes in the g, r, and i bands, with effective wavelengths of 4753, 6369, and 7915 Å, respectively. In this study, we focus exclusively on the g-band light curves, which provide the highest number of observations and the longest temporal baseline (~2000 days). This makes it particularly well-suited for studying AGN optical variability, compared to the more sparsely sampled r and i-band data. Also, we do not use the r and i band light curves to explore the wavelength dependence on τ , as the small separation between the g and r bands limits the ability to identify any significant trends in τ with rest-frame wavelength. To ensure robust variability modeling, we refined the initial sample by selecting only those sources with g-band light curves containing more than 150 epochs. This selection yielded a subsample of 4968 NLSy1 and 5,044 BLSy1 galaxies, which were subjected to further DRW fitting and quality assessment.

Before applying the DRW modeling to the archival light curve data, we performed 3σ clipping on each seasonal segment of the light curves. This procedure helped mitigate the impact of outliers by removing extreme deviations within individual seasons, thereby preserving the intrinsic variability of the sources. In addition, we filtered the light curves by retaining only those epochs with CAT-FLAGS=0, which ensures the exclusion of data points affected by known observational issues such as moonlight contamination, poor image subtraction, saturation, or proximity to charged-coupled device edges. This quality filtering step enhances the reliability of the photometric measurements used in our analysis. The archival ZTF photometric light curves typically contain around \sim 580 high-quality epochs spanning a rest-frame baseline of approximately \sim 2000 days, with a typical photometric uncertainty of 0.047 magnitudes in an



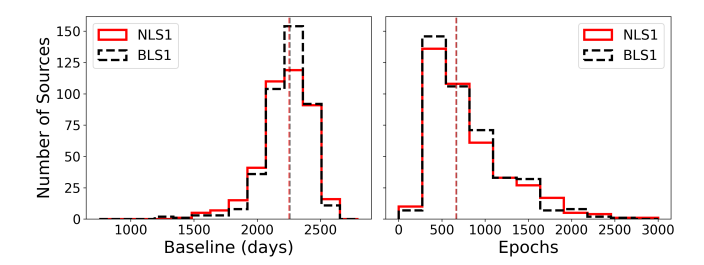


Figure 2. Distribution of the number of epochs and temporal baselines for the ZTF g-band light curves. The left panel shows the archival (normal) photometry, while the right panel shows the forced photometry. Red solid-line histograms represent NLSy1 galaxies (final sample: 1,254), and black dashed-line histograms represent BLSy1 galaxies (final sample: 1,270). For the archival light curves, the median baseline is \sim 2,000 days with a median of 580 high-quality epochs. In comparison, the forced photometry offers an extended baseline of \sim 2,250 days and a higher median of \sim 665 epochs, enabling improved sampling for variability studies.

image. The distribution of epochs and baseline lengths is illustrated in Fig. 2.

2.2 Forced Photometry Data

We also obtained data from the Zwicky Transient Facility Forced Photometry Service (ZFPS), maintained by the ZTF Science Data System team at IPAC/Caltech (Masci et al. 2023), which provides light curves on a request basis. The ZTF forced photometric light curves typically consist of an average of ~665 epochs spanning a baseline of approximately ~2250 days, with a typical photometric uncertainty of 0.035 magnitudes per detection. In forced photometry, the flux of a source is measured at fixed celestial coordinates across all available epochs, regardless of whether the source was independently detected in individual exposures. The forced photometry is carried out on difference images, obtained by subtracting the reference frame from each science exposure, rather than on the original science images. The measured differential flux is then combined with the reference flux to obtain the total calibrated flux. This method ensures consistent flux estimation across time and enables the recovery of faint or transient features. Since the ZFPS includes both recent and archival observations, it is particularly well-suited for generating uniform light curves of variable AGN and improving the reliability of DRW modeling.

Following ZFPS guidelines¹, we performed a series of quality control steps on all forced photometry light curves. Key photometric quantities, such as difference flux and reference magnitude, were converted to flux space, with associated uncertainties propagated accordingly. We computed total fluxes and retained only those epochs with a signal-to-noise ratio (SNR) greater than 3 to ensure the reliability of the measurements. Calibrated magnitudes were then derived, and non-detections or unreliable points were discarded. We restricted the analysis to g-band observations and applied a filter on the PROCSTATUS flag, retaining only values of 0, 59, or 60, which indicate successful or minimally problematic reductions. The PROC-STATUS flag value of 0 indicates successful execution, while 59 and 60 correspond to minor processing flags, slightly elevated photometric uncertainties. These flags do not significantly compromise the quality of the light curves and were found to preserve the reliability of variability measurements without introducing systematic bias. To

3 DATA ANALYSIS: LIGHT CURVE FITTING

AGN light curves have been extensively studied using the DRW framework, which characterizes variability through two key parameters: the damping timescale, τ representing the signal decorrelation timescale, and the variability amplitude, σ (MacLeod et al. 2010). We modeled the light curves using the DRW-based taufit package², developed by Burke et al. (2021). The package is built on the fast Gaussian process solver Celerite (Foreman-Mackey et al. 2017), which uses the following covariance kernel:

$$k(t_{ij}) = 2\sigma_{\text{DRW}}^2 \exp(-t_{ij}/\tau_{\text{DRW}}) + \sigma_i^2 \delta_{ij}$$
(9)

where $t_{ij} = |t_i - t_j|$ is the rest-frame time interval between epochs t_i and t_j . The term where σ_i captures additional white noise that is common to all epochs, often referred to as jitter, to compensate for underestimated or unmodeled uncertainties in the photometric data, with σ_i^2 representing its variance. The Kronecker delta δ_{ij} ensures that the noise is uncorrelated between different epochs. This covariance structure corresponds to the form of the structure function (SF), given by:

$$SF_{ij}^2 = SF_{\infty}^2 (1 - \exp(-t_{ij}/\tau_{DRW}))$$
(10)

where $SF_{\infty} = \sqrt{2}\sigma_{DRW}$ denotes the asymptotic variability amplitude. In the frequency domain, this kernel gives rise to a PSD that transitions from a flat (white noise) regime at low frequencies to a power-law (f^{-2}) decline at high frequencies. The characteristic break frequency at which this transition occurs is defined as:

further mitigate contamination from poor image subtractions or extended structures, we excluded epochs with anomalously high values of *NEARESTREFCHI*, which quantifies the reduced chi-squared of the PSF fit to the nearest reference image; higher values typically indicate poor fits due to nearby sources or extended morphology. As with the archival light curves, we also applied 3σ clipping on a seasonal basis to remove statistical outliers, ensuring consistent treatment across both datasets. These steps yielded clean, high-quality light curves suitable for DRW modeling and time-domain variability analysis.

¹ https://irsa.ipac.caltech.edu/data/ZTF/docs/ztf_forced_
photometry.pdf

https://github.com/burke86/taufit

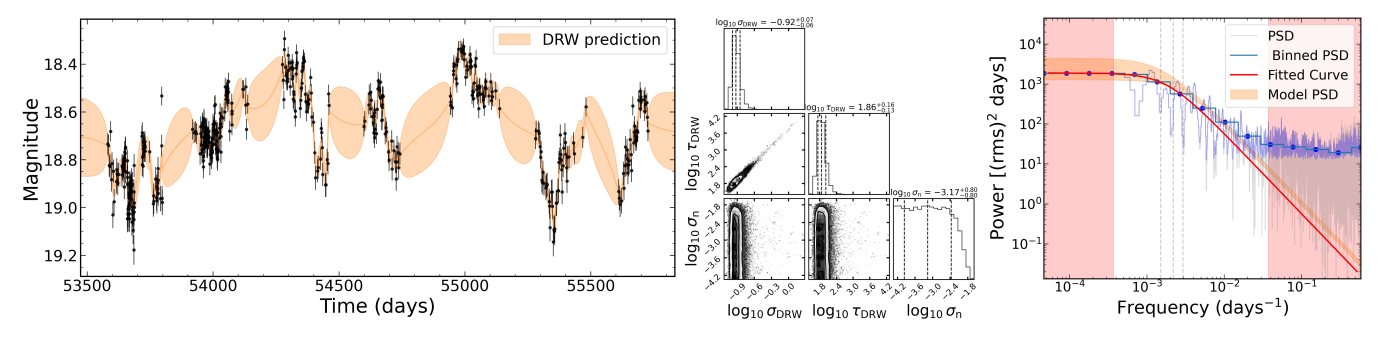


Figure 3. DRW modeling of NLS1 SDSS J000144.85+110959.9 *Left panel:* The g-band light curve of SDSS J000144.85+110959.9 ($M_{\rm BH}=10^{7.703}~M_{\odot}$) DRW model is fitted with $1~\sigma$ uncertainty as orange shaded area. *Right panel:* Power spectral density (PSD) normalized and binned, shown with $1~\sigma$ errors. The best-fit broken power law is overplotted in red and the DRW-based posterior prediction of the PSD is represented by the orange shaded band. The corresponding break frequency f_{br} (from the broken power law fit) and $1/(2\pi\tau_{DRW})$ (from the DRW fitting). The red shaded regions correspond to timescales greater than 20% the light curve length (in panels left lower and right lower) and less than the mean cadence (panel C), where the PSD is not well sampled.

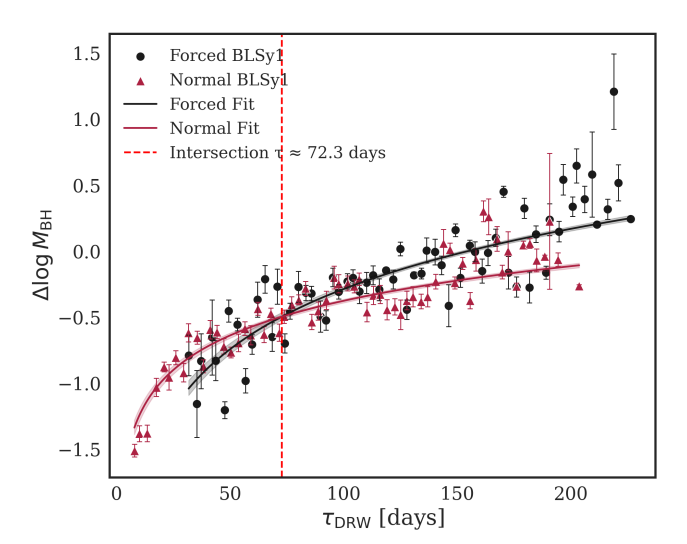


Figure 4. Comparison of the black hole mass offset, defined as $\Delta \log M_{\rm BH} = \log M_{\rm BH,Zhou}^{\rm DRW}$ (equation (8)) - $\log M_{\rm BH}^{\rm SE}$, as a function of the DRW timescale $\tau_{\rm DRW}$, for forced and normal BLSyl light curves. The associated error bars correspond to the median absolute deviation scaled by \sqrt{N} in each bin. The solid black and red lines show the best-fit MCMC regression models for the forced and normal samples, respectively, with shaded regions indicating the $\pm 3\,\sigma$ confidence intervals. The vertical red dashed line marks the intersection point of the two fits at $\tau_{\rm DRW} \approx 72.3$ days, suggesting a potential threshold in timescale-dependent mass discrepancies between the two sampling regimes.

$$f_{\rm br} = \frac{1}{2\pi\tau_{\rm DRW}},\tag{11}$$

which provides a direct link between the time-domain damping timescale and the frequency-domain behavior of the variability.

Within taufit, we also perform Markov chain Monte Carlo (MCMC) sampling via the EMCEE package (Foreman-Mackey et al. 2013), to explore the posterior distributions of the model parameters. We adopted uniform priors for all parameters, used the median of each posterior distribution as the best-fit value, and estimated the 1σ uncertainties from the 16th and 84th percentiles. In our analysis, these priors are uniform (flat) in log-space for the main parameters: the damping timescale (τ_{DRW}), variability amplitude (σ_{DRW}), and white-noise term (σ_i). The prior ranges are automatically set by

taufit based on the light-curve duration, cadence, and photometric precision:

$$\log a \in [\log(0.001 \,(\text{mag err})_{\text{min}}), \, \log(10 \, A)],$$
$$\log c \in [\log(1/(10 \,\text{baseline})), \, \log(1/\text{cadence}_{\text{min}})],$$
$$\log \sigma_{i} \in [-10, \, \log A]$$

where mag err_{min} is the minimum photometric error, A is the total amplitude of variability in the light curve, defined as $A = (\text{mag} + \text{mag} \, \text{err})_{\text{max}} - (\text{mag} - \text{mag} \, \text{err})_{\text{min}}, baseline$ is the total observing period, and $cadence_{\text{min}}$ is the minimum sampling interval. These parameters further constrain the physical quantities of interest, where c corresponds to the damping timescale ($c = 1/\tau_{\text{DRW}}$) and a corresponds to the variability amplitude term ($a = 2\sigma_{DRW}^2$).

In order to reliably constrain the damping time scale (τ_{DRW}) while fitting the light curves, it is important that the duration of the light curve is significantly longer than τ_{DRW} as pointed out by (Kozłowski 2017). For light curves shorter than a few times τ_{DRW} , the measured τ_{DRW} can be systematically biased low and saturated around 20–40% of the light curve duration, with elevated scatter in the measurements. Furthermore, the amplitude of variability σ should also exceed the photometric measurement uncertainties, as emphasized by Burke et al. (2021). This ensures that for low SNR regimes, the inferred τ_{DRW} does not exceed its true intrinsic/true value due to noise-driven fluctuations.

3.1 Final sample

We fitted and analyzed the light curves for each source in our sample using the DRW model described above. Fig. 3 illustrates the results for the NLS1 galaxy SDSS J000144.85+110959.9. The left panel shows the observed light curve along with the predicted curve based on the best-fitting parameters. The middle panel displays a corner plot of the DRW parameters, $\sigma_{\rm DRW}$, $\tau_{\rm DRW}$, and σ_i , obtained using taufit. The right panel presents the PSD of the observed light curve in gray, with the model PSD shown as an orange shaded region representing the 1σ posterior uncertainty. Dashed vertical lines mark the break frequency and its corresponding 1σ confidence interval.

We applied the following criteria to select our final sample:

- (i) Following Kozłowski (2017), we required that each light curve span at least ten times the damping timescale, i.e., baseline > $10 \times \tau_{DRW}$, to ensure robust temporal coverage and minimize biases.
 - (ii) The best-fitting τ_{DRW} must exceed the median cadence to

prevent undersampling related bias (Burke et al. 2021). Additionally, we ensured that the upper bound (84th percentile) of the posterior distribution for τ_{DRW} remained within the light curve duration.

- (iii) We retained only those sources where the intrinsic variability amplitude (σ_{DRW}) exceeded the total noise. Specifically, we required $\sigma_{DRW}^2 > \sigma_i^2 + dy^2$, where σ_i is the jitter component and dy is the median photometric uncertainty of the light curve.
- (iv) Each light curve must include data from at least four distinct ZTF observing seasons, with each season comprising a minimum of 50 epochs. On average, light curves in the final sample span seven seasons and cover a \sim 2000-day baseline.
- (v) We excluded sources whose auto-correlation functions were statistically consistent with Gaussian white noise within the predicted 3σ confidence band (p-value < 0.05).

After applying all selection criteria and estimating black hole masses from the DRW parameters using equation 1, we obtain a distribution of $\log_{10}(M_{\rm BH}/M_{\odot})$ that shows a distinct long tail toward lower masses. This tail consists almost entirely of sources with very short damping timescales, $\tau_{DRW} \lesssim 70$ days. For these cases, the PSD derived from the DRW model appeared nearly flat, as illustrated in Fig. A1. This is most likely due to shorter baseline coverage and sparse sampling in the archival light curves. Such conditions yield poorly constrained DRW parameters, often producing artificially flat model predictions that fail to capture the intrinsic variability. In addition, for the BLSv1 sub-sample, even after incorporating Eddington ratios when calculating black hole masses using the equation 8 relation, the mass offset ($\Delta \log M_{\rm BH} = \log M_{\rm BH,Zhou}^{\rm DRW}({\rm equation~(8)})$ - $\log M_{\rm BH}^{\rm SE}$) shows significant deviations from the expectations based on single-epoch virial estimates (Fig. 4), again indicating that these DRW fits are biased by insufficient data quality.

To address this issue, we retrieved updated light curves from the ZTF Forced Photometry Service (ZFPS) for approximately 307 sources with $\tau_{DRW} \leq 70$ days, incorporating all available observations up to 16 June 2025. Forced photometry offers denser temporal coverage and extended baselines, including an additional ZTF observing season. Although forced photometry may underestimate photometric uncertainties, particularly for highly variable or slightly extended sources, its improved temporal sampling enhances the reliability of DRW modeling. The revised light curves were processed following the procedures described in Masci et al. (2019) and refitted using the same DRW formalism applied to the archival data. A comparison of DRW-based black hole masses from forced and archival photometry is presented in Fig. 4. As seen in Fig. A1, for these same sources the updated fits yield improved damping timescales, and the PSDs are no longer flat, indicating that the intrinsic variability is now better recovered. Hence, for sources with $\tau_{DRW} \leq 70$ days, forced photometry yields systematically more consistent and physically plausible $\Delta \log M_{\rm BH}$ estimates. However, for longer timescales, discrepancies between the two datasets begin to emerge, likely due to growing biases in forced photometric uncertainties.

Additional AGN physical parameters, such as black hole mass, redshift, Fe II strength, and luminosity, are adopted from Paliya et al. (2024). After applying all selection criteria, we obtained a final sample of 1,141 NLSy1s and 1,143 BLSy1s. The two samples remain well matched in the luminosity–redshift (L–z) plane. We find that 81% of these final NLSy1 sources have corresponding BLSy1 counterparts within a matching distance of 0.2. For each source, we compiled key parameters, including the light curve baseline, median cadence, damping timescale ($\tau_{\rm obs}$), variability amplitude ($\sigma_{\rm DRW}$), photometric noise (σ_i), bolometric luminosity ($L_{\rm bol}$), black hole mass ($M_{\rm BH}$), Ed-

dington ratio (λ), and redshift (z). A representative table listing these parameters for a subset of these sources is provided in Appendix 1.

4 RESULTS

We applied the DRW modeling framework to the g-band light curves of 1,141 NLSy1 and 1,143 BLSy1 galaxies using both archival and forced photometry data from the ZTF survey. For each source, we obtained posterior estimates of the DRW parameters, τ_{DRW} , σ_{DRW} , and σ_i . Among these, τ_{DRW} was subsequently used for black hole mass estimation.

4.1 The dependence of $\tau_{\rm DRW}$ on $M_{\rm BH}$

To investigate the relationship between DRW damping timescales and black hole mass, we first compared τ_{DRW} for NLSy1 and BLSy1 galaxies with their single-epoch virial mass estimates. Fig. 5 presents this comparison, where red points correspond to NLSy1 galaxies and black points to BLSy1 galaxies. The top and right panels show the corresponding histograms of $\log M_{\rm BH}^{\rm SE}$ and $au_{
m DRW}$, respectively. Although the two samples exhibit nearly identical τ_{DRW} distributions, their $\log M_{\rm BH}^{\rm SE}$ distributions are clearly distinct, with NLSy1s peaking at lower masses. We then estimated DRW-inferred black hole masses by applying the empirical τ_{DRW} - M_{BH} relation calibrated by Burke et al. (2021), given in equation 1. Fig. 6 shows the distributions of DRW-inferred black hole masses for NLSy1 and BLSv1 galaxies. The solid red and black lines represent the NLSy1 and BLSy1 populations, respectively. The median values are $\log(M_{\rm BH}^{\rm DRW}/M_{\odot}) = 7.94 \pm 0.38$ for NLSy1s and 7.97 \pm 0.36 for BLSy1s. For comparison, the median single-epoch virial mass estimates are 6.81 ± 0.38 for NLSy1s and 7.49 ± 0.41 for BLSy1s, as shown by the red and black shaded histograms in Fig. 6, respectively.

The DRW-based black hole mass distributions for NLSy1s and BLSy1s appear similar, but are systematically higher in both cases than the single-epoch virial estimates. As discussed in Section 1, DRW damping timescales depend on both black hole mass and Eddington ratio. However, the calibration by Burke et al. (2021) assumes a constant Eddington ratio, and neglecting this dependence can lead to overestimated black hole masses in high- $R_{\rm Edd}$ systems.

4.2 The dependence of τ_{DRW} on M_{BH} and R_{Edd}

In our sample, $R_{\rm Edd}$ spans a wide range, from 0.03 to 6.54 for NLSy1s and from 0.001 to 0.95 for BLSy1s, underscoring the need to account for accretion-rate dependence when modeling DRW timescales. To address this, we adopt the multivariate calibration from Zhou et al. (2024) (equation 8), which explicitly incorporates both $M_{\rm BH}$ and $R_{\rm Edd}$ into the DRW framework. We also account for the wavelength dependence of variability timescales by using the g-band central wavelength (4753 Å), corrected to the rest-frame value as $\lambda_{\rm rest} = 4753 \text{Å}/(1+z)$.

 $R_{\rm Edd}$ is typically determined from the bolometric luminosity and the black hole mass. Since our goal is to examine black hole masses in NLSy1s, using the catalog $R_{\rm Edd}$ introduces a cyclic bias, as these values are derived from single-epoch virial masses that may be underestimated due to orientation effects. Consequently, the inferred $R_{\rm Edd}$ values for NLSy1s may also be biased. In BLSy1s, where $R_{\rm Edd}$ spans a narrower range, the mass–damping timescale correlation in equation 1 remains broadly applicable. Several studies have shown that the strength of the optical Fe II emission, quantified by R4570, serves as a more inclination-independent proxy for the Eddington

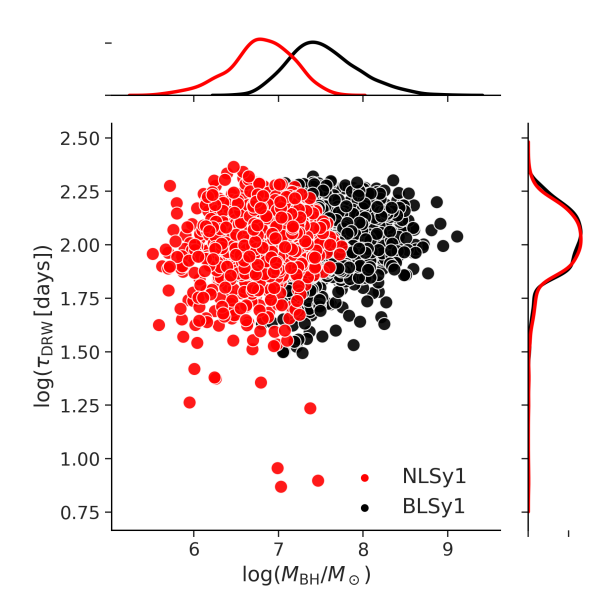


Figure 5. The DRW damping timescale ($\tau_{\rm DRW}$) as a function of single-epoch black hole mass estimates ($M_{\rm BH}$) for the final sample of NLSy1s (red) and BLSy1s (black) galaxies. *Right*: The corresponding distributions of $\tau_{\rm DRW}$, with solid red and dashed black lines for NLSy1s and BLSy1s, respectively. *Upper*: The corresponding distributions are single epoch mass $M_{\rm BH}$, for NLSy1s (red) and BLSy1s (black).

ratio (e.g., Boroson 2002; Shen & Ho 2014). Here, R4570 is defined as the ratio of the Fe II flux in the wavelength range 4434–4684 Å to the flux of the broad component of the H β line. In our analysis, we use R4570 as a proxy for $R_{\rm Edd}$ and explore three strategies to establish a parametric relation between the two.

First, we fit a linear relation between R4570 and $R_{\rm Edd}$ for the BLSy1 sample, for which the catalog $R_{\rm Edd}$ values should be relatively free of any biases. Fig. A2 shows the scatter plot of $log R_{Edd}$ versus R4570 for the full sample of BLSy1 (red) and NLSy1 (blue) galaxies. For the BLSy1s, R4570 was binned in steps of 0.05, and a linear fit to the binned data yields, $log_{10}(R_{Edd}) = 1.66 \times R4570$ - 1.372. The best-fit line for the BLSy1s is shown as a solid black line, with its extrapolation to higher R4570 indicated by the dashed black line. While the fit broadly traces both populations, the substantial scatter, even within the BLSy1 sample, demonstrates that a single-parameter relation between R4570 and $R_{\rm Edd}$ cannot capture the underlying dependencies. Comparing the Paliya et al. (2024) catalog $R_{\rm Edd}$ for the BLSy1 sample with the values reconstructed from the linear relation, reveals a pronounced discrepancy between their distributions. Consequently, we refrain from using this relation to estimate black hole masses. Nevertheless, our analysis emphasizes that the $R_{\rm Edd}$ -R4570 connection is inherently multivariate.

Next, we used the multivariate correlation established by Du et al. (2016) between $\log R_{\rm Edd}$, R4570, and $D_{\rm H\beta}$, where $D_{\rm H\beta}$ is defined as the ratio of the FWHM to the line dispersion of the H β profile. This approach extends beyond the simple linear R4570– $R_{\rm Edd}$ relation by also accounting for the H β line shape, thereby reducing scatter and potential biases in the estimated Eddington ratios. The relation is expressed as

$$\log_{10}(R_{\rm Edd}) = 0.31 - 0.82 \times D_{\rm H\beta} + 0.80 \times R4570, \tag{12}$$

where $D_{H\beta} = \text{FWHM}/\sigma_{H\beta}$, and $\sigma_{H\beta}$ is the dispersion of the broad

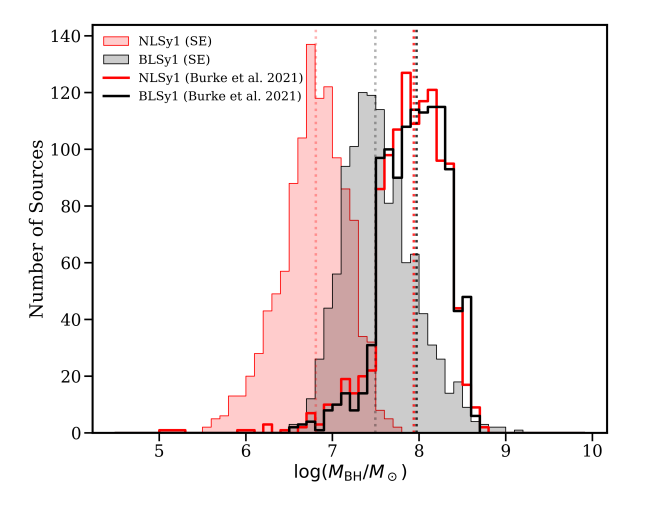


Figure 6. Distribution of black hole masses (log M_{BH}) in units of M_{\odot} for the final sample of NLSy1 (red) and BLSy1 (grey) sources. The single-epoch mass estimates for NLSy1s (shaded red) and BLSy1s (shaded grey) are shown. Solid lines represent mass estimates from the DRW model (as described in equation 1), for NLSy1s (red) and BLSy1s (black). The dashed vertical lines indicate the median values.

 $H\beta$ line. Using this relation, we estimate the Eddington ratio for each NLSy1 source based on its measured Fe II strength and $H\beta$ profile shape. We note that this relation was derived from a sample of only 64 reverberation-mapped AGNs, and thus may be affected by lownumber statistics. However, anchoring the calibration to reverberation mapping-based black hole masses reduces systematic biases relative to single-epoch estimates.

Finally, we also fit the Du et al. (2016) multivariate relation between $\log_{10}(R_{\rm Edd})$, $D_{\rm H\beta}$, and R4570 for our BLSy1 sample of 1143 sources. The $D_{\rm H\beta}$ values were measured using PyQSOFit (Guo et al. 2018). The resulting correlation, $\log_{10}(R_{\rm Edd}) = (-0.33 \pm 0.04) - (0.52 \pm 0.02)$ $D_{\rm H\beta} + (0.59 \pm 0.05)$ R4570 is consistent with the equation 12. Fig. 7 compares the catalog $R_{\rm Edd}$ values with those recalibrated using this relation for the BLSy1 sample. The dashed line indicates the one-to-one correspondence, showing good agreement with modest scatter. Nonetheless, our calibration depends on $R_{\rm Edd}$ values derived from single-epoch virial black hole masses and is therefore more susceptible to systematic biases than the Du et al. (2016) relation.

The $R_{\rm Edd}$ values are then incorporated into equation 8, which uses $\tau_{\rm DRW}$, $R_{\rm Edd}$, and rest-frame wavelength to compute the black hole masses. Our second approach, using the equation 12, yields a median DRW-based black hole mass of $\log(M_{\rm BH}^{\rm DRW}/M_{\odot})=6.25\pm0.65$ for NLSy1s and 7.07 ± 0.67 for BLSy1s. Finally, our third approach, using the adapted Du et al. (2016) relation calibrated for our BLSy1 sample, yields $\log(M_{\rm BH}^{\rm DRW}/M_{\odot})=6.62\pm0.46$ for NLSy1s and 7.20 ± 0.47 for BLSy1s. This suggests that, regardless of the method adopted, the DRW-based masses for NLSy1s remain systematically lower than those for BLSy1s. Fig. 8 shows the distribution of black hole masses ($\log M_{\rm BH}$) for the final sample of NLSy1 (red) and BLSy1 (black) sources obtained using the second approach (equation 12). The single-epoch mass distributions are shown as shaded

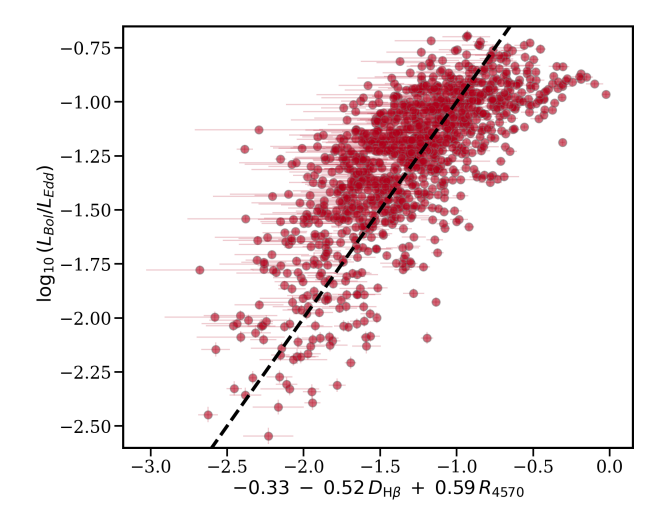


Figure 7. Observed versus modeled Eddington ratios for the BLSy1 sample. The modeled values of $\log_{10}(L_{\rm Bol}/L_{\rm Edd})$ are derived from the best-fitting linear combination of the H β line shape parameter $(D_{\rm H}\beta)$ and R4570. Each point corresponds to an individual source, with horizontal error bars showing measurement uncertainties. The black dashed line marks the one-to-one relation for reference.

histograms, with red and black shading representing the NLSy1 and BLSy1 samples, respectively. The figure clearly illustrates that, after correcting for Eddington ratio effects, NLSy1 galaxies occupy a lower black hole mass regime compared to BLSy1s. We also note that DRW-based masses from equation 12 are systematically lower than the single-epoch estimates, while those from equation 1 are systematically higher, indicating the presence of a residual zero-point offset in DRW-based mass predictions.

5 DISCUSSION

In this study, we measured the black hole masses of NLSy1 galaxies by modeling their optical variability within the framework of the DRW formalism. The widely held view that NLSy1s host relatively low-mass black holes is largely based on virial mass estimates, which rely on the FWHM of the H β line and are therefore sensitive to orientation effects (e.g., Grupe & Mathur 2004). To mitigate these orientation-related biases, we applied the DRW method to model their optical variability using high-cadence g-band light curves from the ZTF survey. Our final sample consists of 1,141 NLSy1 and 1,143 BLSy1 galaxies, matched in the L-z plane. To ensure robust constraints on variability timescales, we made use of both archival and forced photometry light curves from ZTF. The archival light curves generally provide higher SNR measurements, but are limited by source detection thresholds and become incomplete for fainter epochs. While the forced photometry recovers fluxes at fixed source positions even when the source is weakly detected in individual epochs, it provides many more data points and smoother light curve coverage, though at the cost of larger formal photometric errors. The denser sampling it offers is particularly valuable for constraining the DRW damping timescale, τ_{DRW} . Moreover, forced photometry also adds extra observing seasons, effectively extending the temporal baseline and further improving the robustness of the inferred timescales. We recommend using forced photometry, particularly for sources with small τ_{DRW} . Crucially, our main result is unchanged regardless of whether we use forced or archival photom-

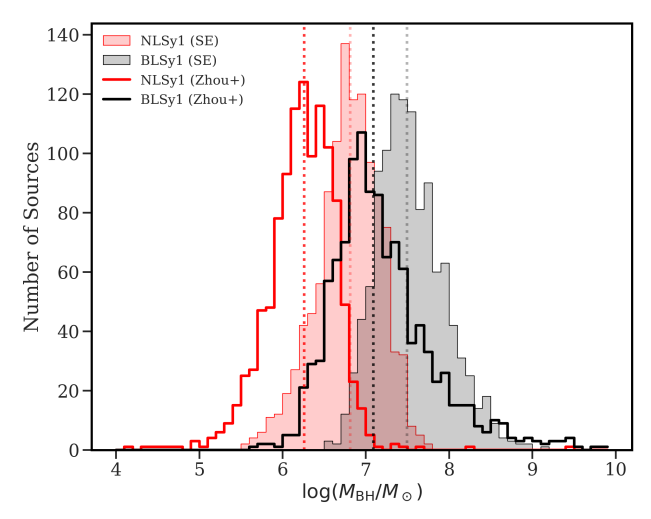


Figure 8. Distribution of black hole masses (log $M_{\rm BH}$) in units of M_{\odot} for the final sample of NLSy1 (red) and BLSy1 (black) sources. The single-epoch mass estimates (shaded) are shown along with DRW-based estimates (solid lines). The dashed vertical lines indicate the median values.

etry. Forced-photometry light curves primarily tighten the inferred $M_{\rm BH}^{\rm DRW}$ distributions by suppressing the extended low-mass tail.

Using the DRW modeling of these light curves, we obtained the two key DRW variability parameters, τ_{DRW} and σ , explored their correlations with physical properties such as $M_{\rm BH}$, $R_{\rm Edd}$, and spectral diagnostics. This analysis revealed that DRW-based black hole mass estimates, when calibrated using the equation 1 under the assumption of a constant $R_{\rm Edd}$, are systematically overestimated for NLSy1s. The calibration yielded median masses of $\log(M_{\rm BH}^{\rm DRW}/M_{\odot}) = 7.94 \pm 0.38$ for NLSy1s and 7.97 ± 0.36 for BLSy1s, significantly exceeding the corresponding SE-based values of 6.81 ± 0.38 and 7.49 ± 0.41 , respectively. While the DRW-based approach for BLSy1 yields broadly consistent results, with only a slight upward bias attributable to their relatively narrow R_{Edd} range (0.001–0.95), it substantially overestimates black hole masses in NLSy1s. This discrepancy arises from the calibration itself in equation 1, which assumes a constant Eddington ratio across all sources, a condition that does not hold for NLSy1s. In our sample, NLSy1s span a much broader and higher range of $R_{\rm Edd}$ values (0.03–6.54), introducing substantial variation in the observed damping timescales. Because τ_{DRW} depends not just on black hole mass, but also on $R_{\rm Edd}$ as suggested by accretion disk theory, ignoring these factors can make a black hole appear more massive, simply because its variability timescale is longer.

To address this discrepancy, we incorporated a multivariate calibration from equation 8 that explicitly includes $\tau_{\rm DRW}$, $R_{\rm Edd}$ and rest-frame wavelength. Since $R_{\rm Edd}$ is defined as the ratio of bolometric to Eddington luminosity, it is inherently linked to the black hole mass. Crucially, using the catalog SE, virial-based black hole masses to compute $R_{\rm Edd}$ and then employing that $R_{\rm Edd}$ in equation 8 to estimate $M_{\rm BH}$ introduces a cyclic bias. To reduce such biases, we explored the use of R4570 (the Fe II /H β flux ratio) as a more robust, inclination-independent proxy for $R_{\rm Edd}$. We first tested the direct correlation between Fe II strength, quantified by R4570, and $R_{\rm Edd}$ for BLSy1s, in line with earlier suggestions that R4570 traces accretion rate. However, in our BLSy1 sample, the simple linear R4570– $R_{\rm Edd}$ relation exhibits substantial intrinsic scatter and yields $R_{\rm Edd}$ distributions that disagree with the Paliya et al. (2024) catalog values. We

therefore conclude that a simple linear dependence on R4570 does not work for reliable mass estimation; the $R_{\rm Edd}$ -R4570 connection is inherently multivariate and requires additional spectral information.

To further refine the estimation, we incorporated broad line region (BLR) kinematic information through the H β line shape parameter $D_{H\beta}$. Applying the relation from equation 12, which links R_{Edd} to both R4570 and $D_{{\rm H}\beta}$, we obtained even lower median masses of $\log(M_{\rm BH}^{\rm DRW}/M_{\odot}) = 6.25 \pm 0.65$ for NLSy1s and 7.07 ± 0.67 for BLSy1s. We also derived an independent recalibration using our own BLSy1 sample, based on the same parameters. This yielded median masses of 6.62 ± 0.46 for NLSy1s and 7.20 ± 0.47 for BLSy1s, consistent within the uncertainties reported by Burke et al. (2021). Both approaches produced similar results, and the mass estimates for BLSy1s remain systematically higher than those for NLSy1s. This persistent offset reinforces the physical distinction between the two populations and highlights the need to correct τ_{DRW} for accretionrate effects in high-R_{Edd} AGNs. Further, the zero-point offsets of the corrected DRW-based masses from all methods relative to the SE estimates, which likely reflect differences in the calibration relations, suggest that further anchoring of DRW-based scalings to reverberation-mapped samples will be needed to resolve the offset. To improve this, future work should tie the DRW scaling relations more directly to reverberation-mapped masses so that a consistent zero-point can be established.

In our sample, we also identify 161 NLSy1 sources with absolute magnitudes brighter than $M_B = -23$, classifying them as narrow-line quasars. These objects tend to have higher black hole masses. However, even after excluding these quasars to isolate a more conservative sample of NLSy1 galaxies, we obtain a median DRW-based black hole mass of $\log(M_{\rm BH}^{\rm DRW}/M_{\odot}) = 6.22 \pm 0.69$, indicating a further downward shift in the mass distribution, as expected for a purer NLSy1 population. Additionally, our sample includes 16 radio-loud NLSy1 galaxies, a small subset that can host relativistic jets and, in principle, alter the optical continuum, variability amplitudes/timescales, and emission line properties. However, this subset is too small to drive the population trends reported here, and our conclusions remain unchanged.

For the initial sample of BLSy1 galaxies, we obtained a median single-epoch virial mass of $\log(M_{\rm BH}/M_{\odot}) = 7.49$. This value, itself, is somewhat lower than typically reported in the literature, likely reflecting the fact that our L-z controlled sample was constructed to match the lower luminosities of the NLSy1s. As a result, the BLSy1 masses in our analysis carry a mild downward bias, which should be considered when comparing to studies based on luminosity-unrestricted BLSy1 samples. Furthermore, our sample also shows an inverse correlation between the variability amplitude and both luminosity and Fe II strength, consistent with the findings of Rakshit & Stalin (2017). Taken together, our findings support a consistent interpretation: the relatively low variability amplitudes and longer damping timescales observed in NLSy1s are more likely driven by their higher accretion rates rather than by systematically larger black hole masses. By incorporating Eddington ratio corrections and adopting inclination-independent proxies such as R4570, we achieve more physically motivated and robust mass estimates. This approach effectively mitigates orientation-induced biases, particularly important given that our sample likely includes sources across a wide range of viewing angles. More broadly, these results underscore the diagnostic power of time-domain variability in constraining accretion physics and black hole demographics in active galaxies.

6 CONCLUSION

In this work, we used optical variability modeling to recalibrate black hole mass estimates for a large sample of NLSy1 and BLSy1 galaxies. By applying the DRW formalism to archival *g*-band light curves from the ZTF survey, we derived characteristic variability timescales and amplitudes for each source. Our analysis demonstrates that DRW–mass scaling relations only depend on blackhole masses, systematically overestimate black hole masses in NLSy1s, primarily because they neglect the impact of Eddington ratio on variability timescales.

To address this limitation, we implemented a multivariate relation that incorporates both the Eddington ratio and the rest-frame wavelength, resulting in more physically consistent mass estimates. Additionally, we employed the Fe II strength (R4570) as an inclination-independent proxy for accretion rate, and further refined the calibration using the H β line shape parameter $D_{\rm H}\beta$ which traces BLR kinematics.

Our findings suggest the interpretation that, as a population, NLSy1 galaxies harbor lower-mass, rapidly accreting black holes compared to their BLSy1 counterparts. More broadly, this study highlights the importance of accounting for accretion-driven variability effects in time-domain analyses and demonstrates the utility of DRW modeling as a powerful tool for probing AGN black hole demographics in large photometric surveys.

7 ACKNOWLEDGMENTS

We thank the anonymous referee for the feedback which has significantly helped to improve the paper. This work makes use of data from the Zwicky Transient Facility (ZTF). The ZTF forced-photometry service was funded under a grant from the Heising-Simons Foundation. Observations were obtained with the Samuel Oschin 48-inch and the 60-inch telescopes at Palomar Observatory as part of the ZTF project (IRSA 2022). ZTF is supported by the National Science Foundation under grants AST-1440341 and AST-2034437, together with a collaboration including Caltech, IPAC, the Weizmann Institute for Science, the Oskar Klein Center at Stockholm University, the University of Maryland, Deutsches Elektronen-Synchrotron and Humboldt University, the TANGO Consortium of Taiwan, the University of Wisconsin-Milwaukee, Trinity College Dublin, Lawrence Livermore National Laboratory, IN2P3, the University of Warwick, Ruhr University Bochum, and Northwestern University, as well as former partners the University of Washington, Los Alamos National Laboratory, and Lawrence Berkeley National Laboratory. Operations are carried out jointly by COO, IPAC, and UW. We acknowledge support from the Department of Science and Technology, India - Science and Engineering Research Board (DST-SERB) in the form of a core research grant (CRG/2022/007884).

DATA AVAILABILITY

All ZTF light-curve data used in this work are publicly available through the ZTF Data Release 23. Forced-photometry light curves can be obtained upon request from the ZTF archive. Spectroscopic data are publicly accessible via the SDSS archive. The reduced parameters underlying this study are provided in machine-readable ASCII/CSV format.

REFERENCES

```
Abdo A. A., et al., 2009, ApJ, 699, 976
Abramowicz M. A., Czerny B., Lasota J. P., Szuszkiewicz E., 1988, ApJ, 332,
    646
Baldi R. D., Capetti A., Robinson A., Laor A., Behar E., 2016, MNRAS, 458,
    L69
Bellm E. C., et al., 2019, PASP, 131, 018002
Bentz M. C., et al., 2006, ApJ, 651, 775
Bentz M. C., Peterson B. M., Netzer H., Pogge R. W., Vestergaard M., 2009,
    ApJ, 697, 160
Bentz M. C., et al., 2013, ApJ, 767, 149
Blandford R. D., McKee C. F., 1982, ApJ, 255, 419
Boller T., Brandt W. N., Fink H., 1996, A&A, 305, 53
Boroson T. A., 2002, ApJ, 565, 78
Boroson T. A., Green R. F., 1992, ApJS, 80, 109
Burke C. J., et al., 2021, Science, 373, 789
Cackett E. M., Bentz M. C., Kara E., 2021, iScience, 24, 102557
Calderone G., Ghisellini G., Colpi M., Dotti M., 2013, MNRAS, 431, 210
Capellupo D. M., Netzer H., Lira P., Trakhtenbrot B., Mejía-Restrepo J., 2015,
    MNRAS, 446, 3427
Capellupo D. M., Netzer H., Lira P., Trakhtenbrot B., Mejía-Restrepo J., 2016,
    MNRAS, 460, 212
Collier S., Peterson B. M., 2001, ApJ, 555, 775
D'Ammando F., et al., 2012, MNRAS, 426, 317
Du P., Wang J.-M., Hu C., Ho L. C., Li Y.-R., Bai J.-M., 2016, ApJ, 818, L14
Foreman-Mackey D., Hogg D. W., Lang D., Goodman J., 2013, PASP, 125,
Foreman-Mackey D., Agol E., Ambikasaran S., Angus R., 2017, AJ, 154, 220
Foschini L., Colpi M., Gallo L., Grupe D., Komossa S., Leighly K., Mathur
    S., eds, 2011, Narrow-Line Seyfert 1 Galaxies and their place in the
Giveon U., Maoz D., Kaspi S., Netzer H., Smith P. S., 1999, MNRAS, 306,
    637
Goodrich R. W., 1989, ApJ, 342, 224
Graham M. J., et al., 2019, PASP, 131, 078001
Grupe D., Mathur S., 2004, ApJ, 606, L41
Guo H., Shen Y., Wang S., 2018, PyOSOFit: Python code to fit the spectrum
    of quasars, Astrophysics Source Code Library, record ascl:1809.008
Kaspi S., Smith P. S., Netzer H., Maoz D., Jannuzi B. T., Giveon U., 2000,
    ApJ, 533, 631
Kaspi S., Maoz D., Netzer H., Peterson B. M., Vestergaard M., Jannuzi B. T.,
    2005, ApJ, 629, 61
Kelly B. C., Bechtold J., Siemiginowska A., 2009, ApJ, 698, 895
Kozłowski S., 2017, A&A, 597, A128
Kozłowski S., et al., 2010, ApJ, 708, 927
Leighly K. M., 1999a, ApJS, 125, 297
Leighly K. M., 1999b, ApJS, 125, 317
MacLeod C. L., et al., 2010, ApJ, 721, 1014
Masci F. J., et al., 2019, PASP, 131, 018003
Masci F. J., et al., 2023, arXiv e-prints, p. arXiv:2305.16279
Mejía-Restrepo J. E., Lira P., Netzer H., Trakhtenbrot B., Capellupo D. M.,
    2018, Nature Astronomy, 2, 63
Osterbrock D. E., Pogge R. W., 1985, ApJ, 297, 166
Paliya V. S., Rajput B., Stalin C. S., Pandey S. B., 2016, ApJ, 819, 121
Paliya V. S., Ajello M., Rakshit S., Mandal A. K., Stalin C. S., Kaur A.,
    Hartmann D., 2018, ApJ, 853, L2
Paliya V. S., Stalin C. S., Domínguez A., Saikia D. J., 2024, MNRAS, 527,
Peterson B. M., 1993, PASP, 105, 247
Rakshit S., Stalin C. S., 2017, ApJ, 842, 96
Scaringi S., et al., 2015, Science Advances, 1, e1500686
Shakura N. I., Sunyaev R. A., 1973, A&A, 24, 337
Shen Y., Ho L. C., 2014, Nature, 513, 210
Simm T., Salvato M., Saglia R., Ponti G., Lanzuisi G., Trakhtenbrot B.,
    Nandra K., Bender R., 2016, A&A, 585, A129
Stone Z., et al., 2022, MNRAS, 514, 164
Suberlak K. L., Ivezić Ž., MacLeod C., 2021, ApJ, 907, 96
```

```
Véron-Cetty M. P., Véron P., Gonçalves A. C., 2001, A&A, 372, 730
Viswanath G., Stalin C. S., Rakshit S., Kurian K. S., Ujjwal K., Gudennavar S. B., Kartha S. S., 2019, ApJ, 881, L24
Wang J.-M., Netzer H., 2003, A&A, 398, 927
Wang T., Brinkmann W., Bergeron J., 1996, A&A, 309, 81
Williams J. K., Gliozzi M., Rudzinsky R. V., 2018, MNRAS, 480, 96
Yu W., Richards G. T., Vogeley M. S., Moreno J., Graham M. J., 2022, ApJ, 936, 132
Zhang H., Yang S., Dai B., 2024, ApJ, 967, L18
Zhou S., Sun M., Cai Z.-Y., Ren G., Wang J.-X., Xue Y., 2024, ApJ, 966, 8
Zu Y., Kochanek C. S., Kozłowski S., Udalski A., 2013, ApJ, 765, 106
```

Sun M., et al., 2020, ApJ, 891, 178

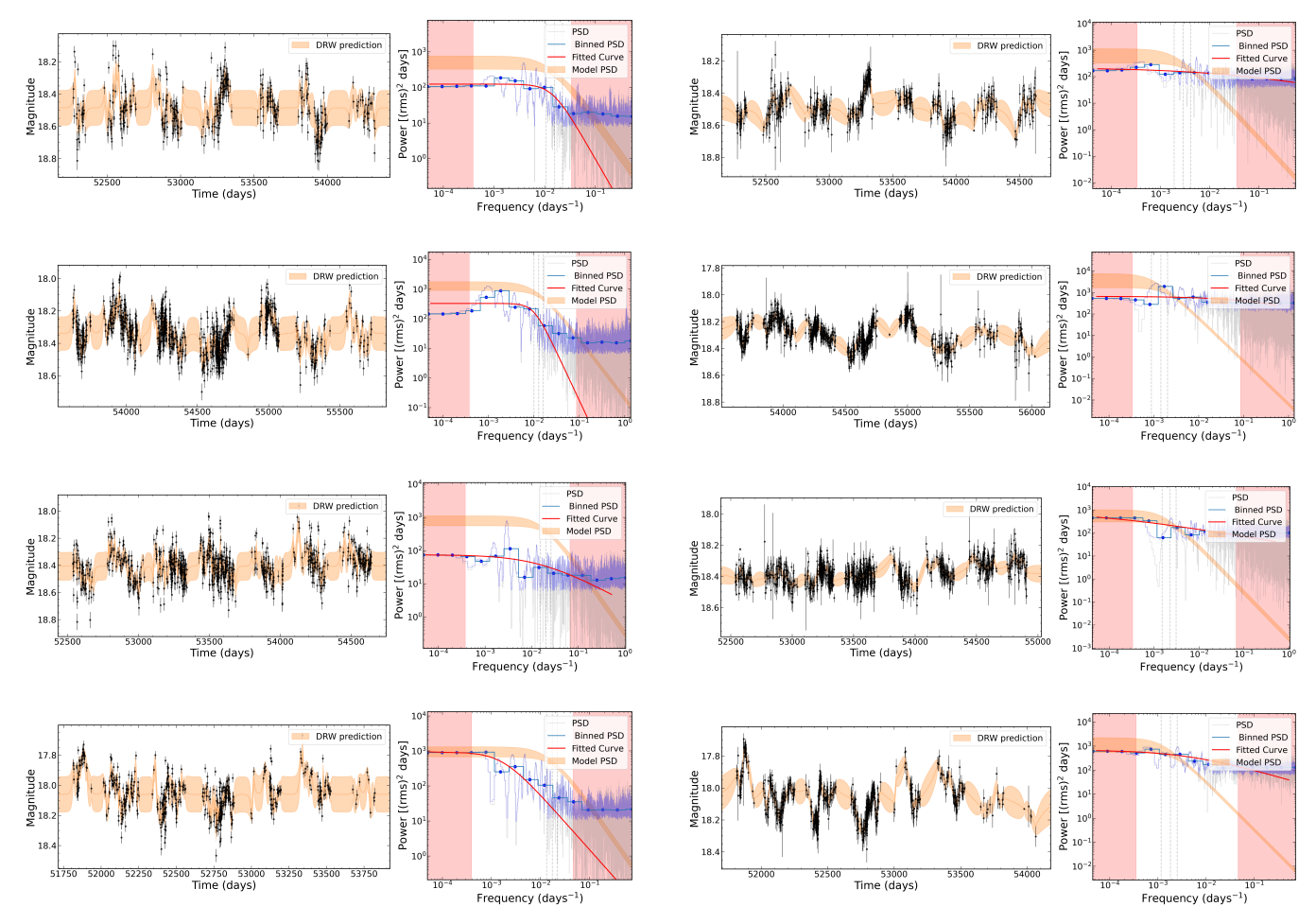


Figure A1. Comparison of ZTF g-band light curves between archival (normal) and forced photometry for four representative sources. Each row corresponds to a different object, identified by its right ascension (RA) and declination (Dec) coordinates: (Top to bottom) (1) SDSSJ121948.93+054531.7 (RA,DEC = 184.9539, 5.758811), (2) SDSSJ130004.09+294624.4 (RA,DEC = 195.0171, 29.77346, (3) SDSSJ144707.05+292025.5 (RA,DEC = 221.7794, 29.34043, and (4) SDSSJ122900.29+272522.2 (RA,DEC = 187.2512, 27.42285. In each pair, the *left panel* shows the light curve and corresponding DRW+PSD fit based on archival photometry, while the *right panel* shows the same analysis using forced photometry. These comparisons highlight the improved sampling and PSD fidelity achieved with forced photometry, enhancing the reliability of DRW-based modeling.

12 Rachana et al.

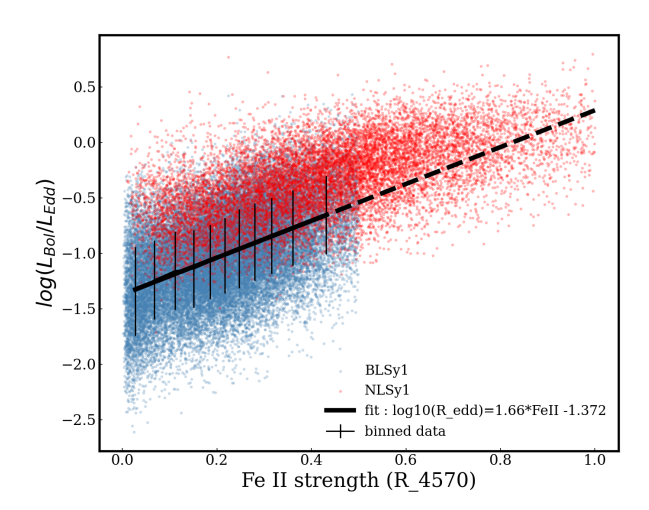


Figure A2. Scatter plot of Eddington ratio and FeII strength (R4570) for the full sample of NLSy1 (blue) and BLSy1 (red) galaxies. The solid black line denotes the best-fit linear relation for the BLSy1 subsample, extended to the NLSy1 regime as a dashed line. The best-fit relation is $log(L_{Bol}/L_{Edd}) = 1.66 \times R_{4570} - 1.372$.

TARI	E OF	FIRST	10	SOURCES

This paper has been typeset from a TEX/LATEX file prepared

		_	Redshift	Redshift Median	log 10 MBH cele	$\log_{10} M_{\rm BH} \sim \log_{10} M_{\rm BH} < E \pm \Delta M_{\rm BH} T_{\rm roc} $	Tree cele		Zitter	-	Bad Region	Bad Region log 10 $L_{\rm Pol} \pm \Delta L_{\rm Pol}$	rec		F i
SDSS Name	RA	DEC	(z)	(z) Error (mag)	([M☉])	([M _☉])	(days)	σ (mag)	(mag)	p-value	(days)	-	$\log_{10} R_{Edd} \pm \Delta R_{Edg} \mid R4570$	R45.	0/
084046.96+400647.0 130.1957 40.1131	130.1957	40.1131	0.23	0.05	80.8	6.61 ± 0.03	110.65	0.07	00.00	0.00	389.94	44.87 ± 0.02	0.12 \pm 0.03 qt	0.76	9
152447.13+520759.1 231.1964 52.1331	231.1964	52.1331	0.16	0.03	69.2	6.70 ± 0.08	77.53	80.0	0.03	0.00	453.15	44.00 ± 0.17	autl	0.34	4
022608.20-005318.8 36.5342 -0.8886	36.5342	-0.8886	0.11	0.03	8.23	6.72 ± 0.05	127.08	0.08	0.00	0.00	413.19	44.23 ± 0.05	or. 20.0 ± 0.0-	0.11	_
163142.49+465243.2 247.9271 46.8787	247.9271	46.8787	0.19	0.07	8.08	6.72 ± 0.08	110.29	0.11	0.00	0.00	403.66	44.04 ± 0.14	-0.82 ± 0.17	0.37	_
123556.54+015728.2 188.9856 1.9578	188.9856	1.9578	0.25	90:0	7.61	6.61 ± 0.14	72.37	60:0	0.03	0.00	421.08	44.25 ± 0.19	-0.50 ± 0.23	0.75	
101832.19+623959.8 154.6341 62.6666	154.6341	9999:79	0.35	0.05	8.13	6.74 ± 0.03	115.76	90:0	0.00	0.00	355.40	45.07 ± 0.04	0.19 ± 0.05	0.47	
133059.08+602128.3 202.7462 60.3579	202.7462	60.3579	0.29	0.05	7.96	6.60 ± 0.14	86.86	60:0	0.00	0.00	359.97	44.22 ± 0.30	-0.52 ± 0.34	0.25	
083949.64+484701.4 129.9569 48.7837	129.9569	48.7837	0.04	0.03	8.09	6.18 ± 0.05	111.81	0.07	0.00	0.00	503.46	43.53 ± 0.11	-0.79 ± 0.12	0.35	· ·
215101.17-083716.2 327.7549 -8.6212	327.7549	-8.6212	0.12	0.02	8.10	6.83 ± 0.01	112.27	0.08	0.01	0.00	417.39	44.80 ± 0.01	-0.17 ± 0.02	0.52	- 7
090628.20+455841.5 136.6175 45.9782 0.18	136.6175	45.9782	0.18	90.0	7.60	6.29 ± 0.07	71.22	0.09	0.00	0.00	406.02	44.17 ± 0.13	-0.27 ± 0.14	0.68	

Table 1: Tabulated properties for the first 10 NLSy1 sources in the sample.